

Electronic structure of superconducting nickelates probed by resonant photoemission spectroscopy

Zhuoyu Chen^{1,2,3*}, Motoki Osada^{1,2,3}, Danfeng Li^{1,3,4}, Emily M. Been^{1,5}, Su-Di Chen^{1,2,3}, Makoto Hashimoto⁶, Donghui Lu⁶, Sung-Kwan Mo⁷, Kyuho Lee^{1,3,5}, Bai Yang Wang^{1,3,5}, Fanny Rodolakis⁸, Jessica L. McChesney⁸, Chunjing Jia¹, Brian Moritz¹, Thomas P. Devereaux^{1,3,9}, Harold Y. Hwang^{1,2,3}, Zhi-Xun Shen^{1,2,3,5*}

¹Stanford Institute for Materials and Energy Sciences, SLAC National Accelerator Laboratory, Menlo Park, CA 94025, USA.

²Department of Applied Physics, Stanford University, Stanford, CA 94305, USA.

³Geballe Laboratory for Advanced Materials, Stanford University, Stanford, CA 94305, USA.

⁴Department of Physics, City University of Hong Kong, Kowloon, Hong Kong

⁵Department of Physics, Stanford University, Stanford, CA 94305, USA.

⁶Stanford Synchrotron Radiation Lightsource, SLAC National Accelerator Laboratory, Menlo Park, California 94025, USA.

⁷Advanced Light Source, Lawrence Berkeley National Lab, Berkeley, California 94720, USA

⁸Advanced Photon Source, Argonne National Laboratory, Lemont, Illinois 60439, USA.

⁹Department of Materials Science and Engineering, Stanford University, Stanford, California 94305, USA.

*Correspondence to: zychen@stanford.edu, zxshen@stanford.edu

The discovery of infinite-layer nickelate superconductors¹⁻³ has spurred enormous interest. While the Ni^{1+} cations possess nominally the same $3d^9$ configuration as Cu^{2+} in high- T_C cuprates⁴, the electronic structure consistencies and variances remain elusive⁵⁻¹⁴, due to the lack of direct experimental probes^{15,16}. Here, we present a soft x-ray photoemission spectroscopy study on both parent and doped infinite-layer Pr-nickelate thin films^{17,18} with a doped perovskite reference. By identifying the Ni character with resonant photoemission and comparison to density function theory + U calculations¹⁹, we estimate $U \sim 5$ eV, smaller than the charge transfer energy $\Delta \sim 8$ eV, in contrast to the cuprates being charge transfer insulators. Near the Fermi level (E_F), we observe a signature of rare-earth spectral intensity in the parent compound, which is depleted upon doping. The parent compound, “self-doped” from rare-earth electrons, exhibits higher density of states at E_F but manifests weaker superconducting instability than the Sr-doped case, demonstrating a complex interplay between the strongly-correlated Ni $3d$ and the weakly-interacting rare-earth $5d$ states in these “oxide-intermetallic” nickelates.

Direct experimental probes of the electronic structure of the novel nickelate superconductors have become the central need since its discovery²⁰. Photoemission spectroscopy provides a measurement of the density of states (DOS) over a wide range of binding energies by analyzing photoelectrons emitted from the material surface²¹. As a highly surface sensitive tool, its application to the nickelate superconductors is especially challenging at the current stage. The infinite-layer phase of superconducting nickelates is formed through epitaxial growth of the perovskite phase, followed with a soft chemistry topotactic reduction. A top capping layer of SrTiO_3 is usually used for the coherent quality of the nickelate films, particularly for the top

layers²². Therefore, the incompatibility with photoemission measurements is two-fold: first, the necessary *ex situ* reduction process introduces surface contamination from the atmosphere; second, the few-unit-cell-thick capping layer impedes the sub-nanometer probe depth of usual angle-resolved photoemission experiments.

To mitigate these obstacles, we conduct photoemission spectroscopy measurements, utilizing the soft x-ray range of photon energy, on the newly developed Pr-based infinite-layer nickelate thin films (i.e. the parent compound PrNiO_2 and the superconducting doped compound $\text{Pr}_{0.8}\text{Sr}_{0.2}\text{NiO}_2$) without capping^{17,18}, together with a perovskite $\text{Pr}_{0.8}\text{Sr}_{0.2}\text{NiO}_3$ thin film for reference. The relatively longer probe depth from the higher photoelectron kinetic energy emitted by soft x-ray helps alleviate sensitivity to surface contamination. The surface free from capping enables a direct measurement of the DOS of the nickelate films without the influence of the photoemission signal from the cap.

Figure 1a shows the measurement configuration of our experiment. Incident photons with circular polarization is angled 35° to grazing, such that both in-plane and out-of-plane electron orbitals can be excited. The photoelectron analyzer is positioned near the normal direction of the thin film surface. Due to the inevitable *ex situ* exposure before the measurement, we have not observed angle-resolved dispersive features in the measured spectra for the infinite-layer samples. The current to the ground is measured simultaneously for the total electron yield of x-ray absorption spectroscopy (XAS). Figure 1b,c exhibit the XAS for Ni L_3 and O K edges, respectively. On the Ni L_3 edge, while the $\text{Pr}_{0.8}\text{Sr}_{0.2}\text{NiO}_3$ sample manifest a different line shape, as expected for a different Ni oxidization state, the $\text{Pr}_{0.8}\text{Sr}_{0.2}\text{NiO}_2$ and PrNiO_2 samples show largely similar line shape with about 0.1~0.2 eV shift between each other. The peak for the doped sample appears to be about 0.1 eV broader than the parent sample. This energy shift and

broadening change might be related to 1) a chemical potential shift, and 2) increased hybridization in the doped compound¹⁶. On the O K edge, the suppression of the strong pre-peak in the $\text{Pr}_{0.8}\text{Sr}_{0.2}\text{NiO}_3$ sample after reduction reflects the shift of oxygen partial DOS away from the Fermi level for both infinite-layer samples¹⁵. Figure 1d shows the x-ray photoelectron spectroscopy (XPS) for O K edge. These O K peaks have similar peak width with a relative shift between one another. Relative to PrNiO_2 , the peaks for $\text{Pr}_{0.8}\text{Sr}_{0.2}\text{NiO}_2$ and $\text{Pr}_{0.8}\text{Sr}_{0.2}\text{NiO}_3$ shift around 0.2 eV and 0.6 eV, respectively. These peak shifts are likely due to chemical potential shifts. Additional XPS and XAS data are presented in supplementary information Fig. S1-S2.

To probe the chemical potential shifts between these three samples, photoemission spectra for the valence band DOS are shown in Fig. 2a. While the line shape of the perovskite phase sample $\text{Pr}_{0.8}\text{Sr}_{0.2}\text{NiO}_3$ is quite different, the two infinite-layer-phase curves are almost identical with 0.2 eV of overall energy shift. If we use the midpoint (intensity = 0.5, circles in Fig. 2a) as a representative energy of the valence band top, $\text{Pr}_{0.8}\text{Sr}_{0.2}\text{NiO}_3$ has a 0.6 eV energy shift with respect to PrNiO_2 . The same energy shift is also observed for the peaks of the valence band DOS (diamonds in Fig. 2a). The 0.2 eV and 0.6 eV values are consistent with the oxygen K core level XPS peak shifts (Fig. 1d); thus, we attribute them to chemical potential changes coming from hole doping.

To further analyze the DOS, we compare the PrNiO_2 experimental data with density functional theory calculation (local density approximation with on-site Coulomb interaction potential U , hereafter LDA+ U) with different U values¹⁹, as shown in Fig. 2b. By varying U , the Ni 3d partial DOS envelop (blue) continually shifts to higher binding energy, while the O 2p partial DOS envelop (red) remains mostly at the same position with some spreading towards E_F near the high- U end. When $U = 0$ (non-interacting), the upper tail of the Ni 3d envelop crosses E_F , but a gap is

formed when $U = 3$ eV. The overlapping between Ni and O is small when U is low and becomes significant when U is larger than 6 eV. By Gaussian peak fitting, we found there are two prominent features in the experimental DOS, matching the Ni $3d$ and O $2p$ partial DOS envelopes found in the LDA+ U simulations. The Ni partial DOS correspondence is justified by resonant photoemission data to be discussed in Fig. 3. The binding energies of prominent features of the simulated partial DOS are quantified and plotted as a function of U in Fig. 2c. The comparison of the Ni feature with experimental fitted center of weight values gives an estimate of $U = (5 \pm 1)$ eV. The error is estimated based on an analysis of the overlap between experimental and simulated Ni partial DOS as a function of U , as discussed in the supplementary information Fig. S3.

With the understanding of the infinite-layer electronic structure, here we discuss the differences among cuprates, infinite-layer nickelates, and perovskite nickelates, as illustrated in Fig. 2d. While cuprates⁴ are known to be charge transfer insulators where the charge transfer energy Δ is far smaller than the Hubbard U , infinite-layer nickelates are in the opposite regime, having $U \sim 5$ eV and $\Delta \sim U + (E_{\text{Ni}3d} - E_{\text{O}2p}) \approx 8$ eV, where $E_{\text{Ni}3d}$ and $E_{\text{O}2p}$ are the experimental fitted binding energies of the Ni $3d$ and O $2p$ features (Fig. 2c), respectively. For perovskite nickelates, previous studies^{23–25} have shown that it is effectively a “negative charge transfer” compound with dominating O $2p$ states crossing E_F : the significant number of empty O $2p$ states above E_F gives rise to the strong pre-peak in XAS near the O K edge (Fig. 1c). As such, contrasting to cuprates and to a lesser extend perovskite nickelates, the states near the Fermi level in infinite-layer nickelates have more dominating $3d$ character than $2p$ character.

To clarify the elemental specificity of states observed in the photoemission spectra, we performed resonant photoemission spectroscopy measurements near the Ni L_3 absorption edge,

which enhances spectral intensity from Ni $3d$ states through additional emission channels allowed in the resonance process. Figure 3a shows an example comparison of the detected photoemission signals between the off- and on-resonant cases. The off-resonant (before the edge, black, corresponding to #0 photon energy shown in Fig. 3c) curve represents a typical photoemission spectrum, with both valence band and Pr $5p$ states observed. The on-resonant curve (post-edge, green, corresponding to #4 in Fig. 3c) apparently has increased intensity. The increased part of the intensity, as shown by the thick purple curve (#4 – #0), comes purely from the additional channels related to Ni absorption, and thus represent Ni response only. This is verified by a complete absence of the Pr $5p$ feature in the subtracted curve.

However, as illustrated in Fig. 3b, this pure Ni response also has two different origins. After absorption, an electron from the Ni L_3 core level is excited to an empty state above E_F , leaving a hole in the core level. Following this step, there are two possibilities²⁶: 1) the excited electron refills the core hole and transfers the energy to a valence electron, which is then emitted with a final state being the same as for a regular photoemission process – the interference of these two channels gives rise to a resonance effect; 2) an electron in an occupied state fills the core hole and energy is transferred to another electron in an occupied state – the emitted electron has a kinetic energy independent of photon energy, thus is an Auger electron rather than a photoelectron. We need to separate the signals with these two different origins to obtain resonant photoemission spectra. Figure 3c displays the photoemission intensity as a function of binding energy with different photon energies. Auger signals have constant kinetic energy, and therefore form diagonal features in Fig. 3c, distinct from photoemission signals with constant binding energy. For better separation of these two parts, we choose to analyze spectra with photon energy higher than the absorption edge (#1 to #6). Gaussian peak fitting analysis is shown in Fig. 3d,

where one can see clear separation of features with constant and varying binding energies, representing Ni $3d$ states (blue) and Ni $L_3M_{4,5}M_{4,5}$ Auger electrons (green), respectively²⁷. The identification of Ni $3d$ states here verified the assignment of orbital characters in Fig. 2. Other results of resonant photoemission are shown in Fig. S4.

Now we turn to discuss the near- E_F features. Figure 4a shows the higher-statistics photoemission spectra close to E_F . Comparing with the perovskite compound, a significant suppression of spectral intensity near E_F is observed in the infinite-layer samples. As discussed earlier, near- E_F states for the perovskite compound are dominated by O $2p$ orbitals. A prominent “step” feature (between -0.5 eV and E_F) observed here is consistent with the observation of a strong pre-peak in the XAS near O K edge in Fig. 1c, both of which come from O $2p$, but the former represents occupied states while the latter corresponds to unoccupied states. These observations support the effective “negative charge transfer” picture for the perovskite nickelate. In the infinite-layer parent compound, analysis above have shown Ni $3d$ states are pushed away from E_F due to finite U . An overall analysis of the LDA+ U simulation near E_F , with Pr characteristics and cross sections²⁸ considered, is shown in Fig. 4b. As U increases from zero, the Ni $3d$ partial DOS drops significantly. On the other hand, weakly interacting three-dimensional Pr $5d$ states have small but finite DOS crossing E_F , and dominate the DOS near $U \sim 5$ eV. Experimentally, a very small but finite “Fermi step” is indeed observed near E_F for the parent compound (inset of Fig. 4a). With the same measurement geometry, this small feature is depleted by Sr hole-type doping. This indicates that it is an electron-type pocket and must be related to the Pr $5d$ orbital, as illustrated in Fig. 4c. The existence of Pr $5d$ states near E_F presents a sharp contrast to the cuprates, in which rare-earth states are far above E_F . The ultra-low spectral intensity for the doped infinite-layer sample might have a few origins: 1) Ni $3d$ has low spectral

weight near E_F with even 0.2 eV shift of chemical potential as pointed out by LDA+U simulation; 2) the cross section of Ni $3d$ is significantly lower than rare-earth $5d$; 3) surface effects arising from *ex situ* sample loading and the topotactic reduction process.

Previous reports^{2,3,18,29} point out that both parent and Sr-doped infinite-layer nickelates exhibit metallic behavior with similar order of magnitude conductivity, in contrast to cuprates where 20%-hole doping gives rise to ~ 100 times enhancement of conductivity³⁰. While the Sr doping provides hole-type carriers to the system, the parent infinite-layer nickelate is “self-doped” because of the small electron pocket (unlike the parent perovskite nickelate also being “self-doped” but of hole-like character via negative charge transfer²³). Intriguingly, our observation indicate that the “self-doped” parent infinite-layer compound has higher DOS at E_F (Fig. 4a inset) due to the existence of additional Pr $5d$ channel, yet it manifests weaker superconducting instability compared to the Sr-doped compound^{2,3,18,29}. This property, distinct from conventional superconductors in which higher DOS always gives rise to stronger superconductivity, implies that the superconductivity in the nickelates has an unconventional origin. Within the group of hole-doped unconventional superconductors, our results hint two possible reasons for the significantly lower transition temperature (T_C) of the nickelates than the cuprates: 1) the proximity to weakly-interacting rare-earth $5d$ states affects the pairing strength; 2) the absence of O $2p$ partial DOS near E_F might hinder coupling to other bosonic degrees of freedom, e.g. phonons, that potentially assist superconductivity.

In summary, although the infinite-layer nickelates and cuprates are isostructural and have nominally the same $3d^9$ configuration, we have shown evidence that their electronic structures are dissimilar in two aspects. First, the nickelates have smaller U than Δ , making the NiO_2 planes “Mott insulating” with states near E_F of mainly $3d$ character, while cuprates as charge transfer

insulators are the opposite, indicating a correlation between O $2p$ associated bosonic degrees of freedom and higher T_C . Second, in addition to the strongly correlated NiO_2 planes, weakly-interacting rare-earth $5d$ states near E_F play an essential role for conductivity but a complex role for superconductivity, in sharp contrast to cuprates.

Methods

Sample preparation. Infinite-layer nickelate films of 6 nm were synthesized by pulsed laser deposition, followed by a subsequent topotactic reduction reaction. It has been found that an upper SrTiO_3 cap was unnecessary for stabilizing a uniform single-crystalline infinite-layer structure for Pr-based nickelates, possibly due to a better lattice matching to the STO substrate and a larger tolerance factor^{17,18}. Therefore, precursor perovskite films were synthesized without an SrTiO_3 cap at 570 °C substrate temperature. The laser fluence and oxygen pressure for the growth of PrNiO_3 and $\text{Pr}_{0.8}\text{Sr}_{0.2}\text{NiO}_3$ are 1.39 J/cm², 200 mTorr and 2.19 J/cm², 250 mTorr, respectively. The laser repetition was 4 Hz. The perovskite film measured here is 9 nm thick. The topotactic reduction is done *ex situ* by sealing CaH_2 and the precursor perovskite film in a glass tube and heating in a tube furnace at 240 °C for 60 min. More details about synthesis and characterizations are reported earlier^{17,18}.

Spectroscopy measurements. Photoemission spectroscopy, XPS, and XAS measurements were performed at the Advanced Photon Source (APS) Sector 29-ID angle-resolved photoemission spectroscopy end station. Samples prepared at Stanford were sealed within vacuum glass tubes for shipment to APS. At the beamline, samples were mounted using tantalum foils in air and loaded into the measurement chamber. We found pre-annealing in UHV below 250 °C (temperatures higher than this could lead to sample decomposition) before measurement does not

give noticeable improvement to spectroscopic data quality. The measurement temperature for the data shown is lower than 20 K. We did not observe angle-dependent dispersion of photoemission intensity for the infinite-layer samples.

Theoretical calculations. LDA+U calculations were performed using the GGA method and the simplified version from Cococcioni and de Gironcoli³¹, as implemented in QUANTUM ESPRESSO³².

Data Availability

The data that support the findings of this study are available from the corresponding authors upon reasonable request.

Acknowledgements

We thank Wei-Sheng Lee and Haiyu Lu for discussions. The work at SLAC and Stanford was supported by the U.S. Department of Energy (DOE), Office of Basic Energy Sciences, Division of Materials Sciences and Engineering (contract No. DE-AC02-76SF00515) and the Gordon and Betty Moore Foundation’s Emergent Phenomena in Quantum Systems Initiative (grant No. GBMF9072, synthesis equipment). This research used resources of the Advanced Photon Source, a DOE user facility operated by Argonne National Laboratory under contract No. DE-AC02-06CH11357. The work at LBNL was supported by US DOE under contract No. DE-AC02-05CH11231. Danfeng Li acknowledges the financial support from City University of Hong Kong under Project 9610500.

Author Contribution

Z.C., H.Y.H, and Z.X.S. conceived the experiment. Z.C., S.D.C., M.H., D.Lu, and S.K.M. performed soft x-ray photoemission measurements remotely with significant assistance from F.R. and J.L.M. at the beamline. M.O., D.Li, with assistance from K.L. and B.Y.W., provided samples. E.M.B., C.J., B.M., and T.P.D. performed LDA+U simulations and provided theoretical interpretation. Z.C. wrote the manuscript with input from all authors.

Competing interests

The authors declare no competing interests.

Reference

1. Li, D. *et al.* Superconductivity in an infinite-layer nickelate. *Nature* **572**, 624–627 (2019).
2. Li, D. *et al.* Superconducting Dome in $\text{Nd}_{1-x}\text{Sr}_x\text{NiO}_2$ Infinite Layer Films. *Phys. Rev. Lett.* **125**, 27001 (2020).
3. Zeng, S. *et al.* Phase Diagram and Superconducting Dome of Infinite-Layer $\text{Nd}_{1-x}\text{Sr}_x\text{NiO}_2$ Thin Films. *Phys. Rev. Lett.* **125**, 147003 (2020).
4. Keimer, B., Kivelson, S. A., Norman, M. R., Uchida, S. & Zaanen, J. From quantum matter to high-temperature superconductivity in copper oxides. *Nature* **518**, 179–186 (2015).
5. Anisimov, V. I., Bukhvalov, D. & Rice, T. M. Electronic structure of possible nickelate analogs to the cuprates. *Phys. Rev. B* **59**, 7901–7906 (1999).
6. Lee, K. W. & Pickett, W. E. Infinite-layer LaNiO_2 : Ni^{1+} is not Cu^{2+} . *Phys. Rev. B* **70**, 165109 (2004).

7. Botana, A. S. & Norman, M. R. Similarities and Differences between LaNiO_2 and CaCuO_2 and Implications for Superconductivity. *Phys. Rev. X* **10**, 011024 (2020).
8. Karp, J. *et al.* Many-Body Electronic Structure of NdNiO_2 and CaCuO_2 . *Phys. Rev. X* **10**, 021061 (2020).
9. Jiang, M., Berciu, M. & Sawatzky, G. A. Critical Nature of the Ni Spin State in Doped NdNiO_2 . *Phys. Rev. Lett.* **124**, 207004 (2020).
10. Sakakibara, H. *et al.* Model Construction and a Possibility of Cupratelike Pairing in a New d^9 Nickelate Superconductor $(\text{Nd,Sr})\text{NiO}_2$. *Phys. Rev. Lett.* **125**, 77003 (2020).
11. Jiang, P., Si, L., Liao, Z. & Zhong, Z. Electronic structure of rare-earth infinite-layer RNiO_2 ($\text{R}=\text{La,Nd}$). *Phys. Rev. B* **100**, 201106(R) (2019).
12. Choi, M. Y., Lee, K. W. & Pickett, W. E. Role of $4f$ states in infinite-layer NdNiO_2 . *Phys. Rev. B* **101**, 020503(R) (2020).
13. Wu, X. *et al.* Robust $d_{x^2-y^2}$ -wave superconductivity of infinite-layer nickelates. *Phys. Rev. B* **101**, 060504(R) (2020).
14. Gu, Y., Zhu, S., Wang, X., Hu, J. & Chen, H. A substantial hybridization between correlated Ni- d orbital and itinerant electrons in infinite-layer nickelates. *Commun. Phys.* **3**, 84 (2020).
15. Hepting, M. *et al.* Electronic structure of the parent compound of superconducting infinite-layer nickelates. *Nat. Mater.* **19**, 381–385 (2020).
16. Goodge, B. H. *et al.* Doping evolution of the Mott-Hubbard landscape in infinite-layer nickelates. *Proc. Natl. Acad. Sci. U. S. A.* **118**, e2007683118 (2021).
17. Osada, M. *et al.* A Superconducting Praseodymium Nickelate with Infinite Layer Structure. *Nano Lett.* **20**, 5735–5740 (2020).

18. Osada, M., Wang, B. Y., Lee, K., Li, D. & Hwang, H. Y. Phase diagram of infinite layer praseodymium nickelate $\text{Pr}_{1-x}\text{Sr}_x\text{NiO}_2$ thin films. *Phys. Rev. Mater.* **4**, 121801(R) (2020).
19. Been, E. *et al.* Electronic Structure Trends Across the Rare-Earth Series in Superconducting Infinite-Layer Nickelates. *Phys. Rev. X* **11**, 11050 (2021).
20. Norman, M. R. Entering the Nickel Age of Superconductivity. *Physics* **13**, 85 (2020).
21. Lu, D. *et al.* Angle-Resolved Photoemission Studies of Quantum Materials. *Annu. Rev. Condens. Matter Phys.* **3**, 129–167 (2012).
22. Lee, K. *et al.* Aspects of the synthesis of thin film superconducting infinite-layer nickelates. *APL Mater.* **8**, 041107 (2020).
23. Bisogni, V. *et al.* Ground-state oxygen holes and the metal-insulator transition in the negative charge-transfer rare-earth nickelates. *Nat. Commun.* **7**, 13017 (2016).
24. Nowadnick, E. A. *et al.* Quantifying electronic correlation strength in a complex oxide: A combined DMFT and ARPES study of LaNiO_3 . *Phys. Rev. B* **92**, 245109 (2015).
25. Berner, G. *et al.* Dimensionality-tuned electronic structure of nickelate superlattices explored by soft-x-ray angle-resolved photoelectron spectroscopy. *Phys. Rev. B* **92**, 125130 (2015).
26. Guillot, C. *et al.* Resonant Photoemission in Nickel Metal. *Phys. Rev. Lett.* **39**, 1632–1635 (1977).
27. Yin, L. I., Yellin, E. & Adler, I. X-Ray Excited LMM Auger Spectra of Copper, Nickel, and Iron. *J. Appl. Phys.* **42**, 3595 (1971).
28. Scofield, J. H. Theoretical Photoionization Cross Sections From 1 To 1500 keV. *United States*. <https://doi.org/10.2172/4545040> (1973).
29. Wang, B. Y. *et al.* Isotropic Pauli-limited superconductivity in the infinite-layer nickelate

- $\text{Nd}_{0.775}\text{Sr}_{0.225}\text{NiO}_2$. *Nat. Phys.* **17**, 473–477 (2021).
30. Takagi, H. *et al.* Superconductor-to-nonsuperconductor transition in $(\text{La}_{1-x}\text{Sr}_x)_2\text{CuO}_4$ as investigated by transport and magnetic measurements. *Phys. Rev. B* **40**, 2254-2261 (1989).
 31. Cococcioni, M. & De Gironcoli, S. Linear response approach to the calculation of the effective interaction parameters in the LDA+U method. *Phys. Rev. B* **71**, 035105 (2005).
 32. Giannozzi, P. *et al.* QUANTUM ESPRESSO: A modular and open-source software project for quantum simulations of materials. *J. Phys. Condens. Matter* **21**, 395502 (2009).

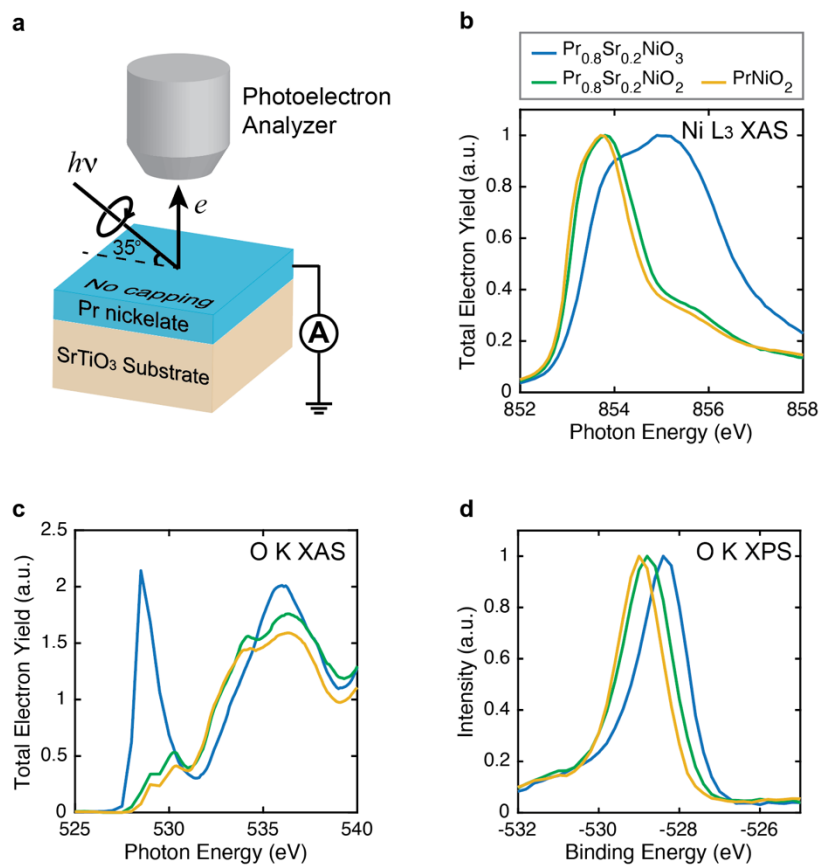


Figure 1 | X-ray absorption and photoelectron spectroscopy. **a.** Schematic diagram of the experimental setup. **b and c.** X-ray absorption spectra of the three different samples near the nickel L₃ edge and oxygen K edge, respectively. **d.** Oxygen K x-ray photoelectron spectroscopy peaks of the three samples.

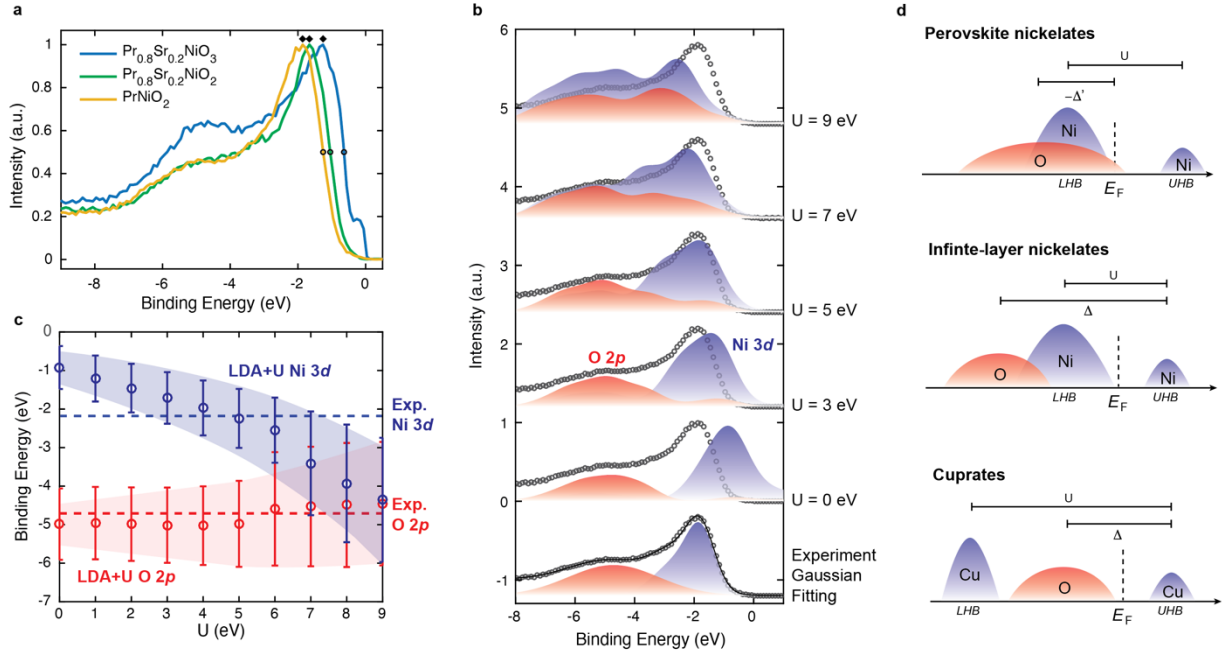


Figure 2 | Density of states. **a.** Photoemission spectra of the three samples with maximum intensity normalized to one. Diamonds and circles represent peak and midpoint positions, respectively. Measurement photon energy is 260 eV. **b.** LDA+U results with different representative U values compared with Gaussian fitting of experiment. Grey circles are experimental data for PrNiO_2 . Black solid curve is the Gaussian fitting. Blue shaded envelopes represent Ni 3d related states. Note that for the experiment Gaussian fitting the blue shaded envelop consist of two Gaussian peaks. Red shaded envelopes represent O 2p related states. The simulated shaded envelopes are with 0.5 eV broadening. **c.** Binding energies of the Ni 3d and O 2p prominent features (center of weight, only features with $> 40\%$ of peak intensity are counted) as a function of U , based on LDA+U simulation. Error bars represent standard deviations. Dashed lines correspond to values from Gaussian fitting of experiment. **d.** Schematic diagrams of the electronic structure of cuprates, infinite-layer nickelates, and perovskite nickelates.

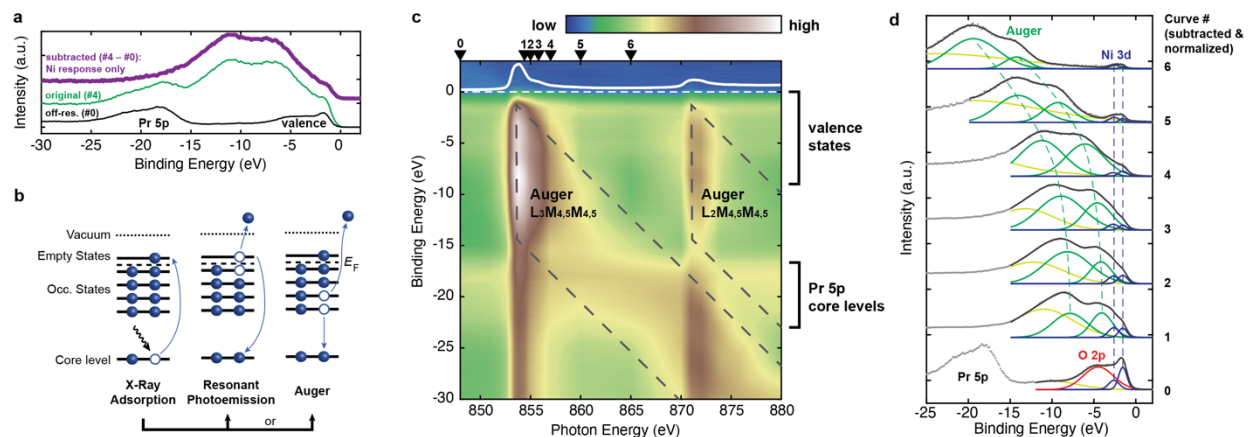


Figure 3 | Resonant photoemission spectra at Ni edges. **a.** Spectra for photon energies of 848 eV (black, off-resonant, corresponding to #0 in c), 857 eV (green, adoption enhanced, corresponding to #4 in c), and the subtracted spectrum ($\#4 - \#0$). The subtracted curve represent response from Ni states only. **b.** Schematic diagrams of the two possible two-step processes that begins with x-ray absorption. **c.** Spectra at different photon energies in color plot. Areas marked by dashed lines corresponds to Auger dominant regions. **d.** Spectra with Gaussian fitting analysis for photon energies marked by #0 to #6 shown with triangles in c. Blue, red, and green curves represent Ni states, O states, and Auger features, respectively. Grey dots are experimental data. #1 to #6 curves shown here are after subtracted with #0 curve and normalized with the maximum intensity for clarity of presentation. The #0 off-resonant curve is original, same as that shown in a.

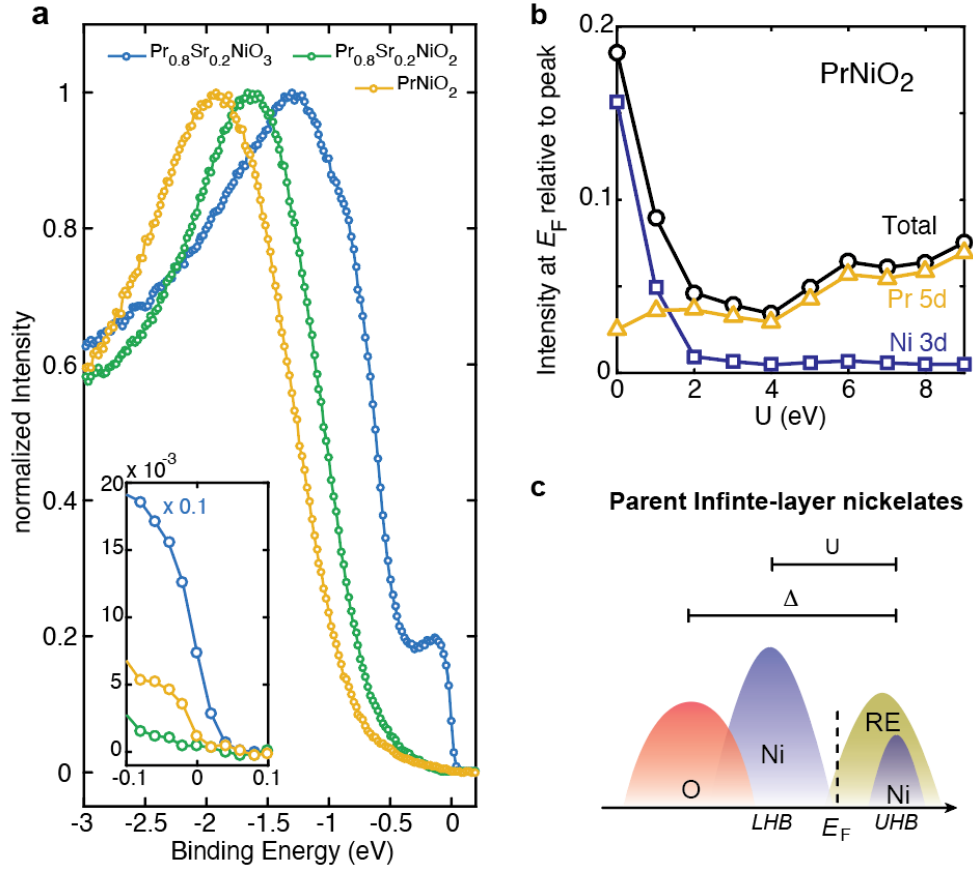


Figure 4 | Near- E_F features. **a.** Photoemission spectra near E_F of the three samples with maximum intensity normalized to one. Inset is a magnification of a small region around E_F . Measurement photon energy is 260 eV. **b.** LDA+U simulation results of intensity at E_F of different orbitals as a function of U with cross sections considered. The broadening utilized here is 34 meV. **c.** Schematic diagram of electronic structure for parent infinite-layer nickelates. RE: rare earth.

Supplementary information for

Electronic structure of superconducting nickelates probed by resonant photoemission spectroscopy

Zhuoyu Chen^{1,2,3*}, Motoki Osada^{1,2,3}, Danfeng Li^{1,3,4}, Emily M. Been^{1,5}, Su-Di Chen^{1,2,3}, Makoto Hashimoto⁶, Donghui Lu⁶, Sung-Kwan Mo⁷, Kyuho Lee^{1,3,5}, Bai Yang Wang^{1,3,5}, Fanny Rodolakis⁸, Jessica L. McChesney⁸, Chunjing Jia¹, Brian Moritz¹, Thomas P. Devereaux^{1,3,9}, Harold Y. Hwang^{1,2,3}, Zhi-Xun Shen^{1,2,3,5*}

¹Stanford Institute for Materials and Energy Sciences, SLAC National Accelerator Laboratory, Menlo Park, CA 94025, USA.

²Department of Applied Physics, Stanford University, Stanford, CA 94305, USA.

³Geballe Laboratory for Advanced Materials, Stanford University, Stanford, CA 94305, USA.

⁴Department of Physics, City University of Hong Kong, Kowloon, Hong Kong

⁵Department of Physics, Stanford University, Stanford, CA 94305, USA.

⁶Stanford Synchrotron Radiation Lightsource, SLAC National Accelerator Laboratory, Menlo Park, California 94025, USA.

⁷Advanced Light Source, Lawrence Berkeley National Lab, Berkeley, California 94720, USA

⁸Advanced Photon Source, Argonne National Laboratory, Lemont, Illinois 60439, USA.

⁹Department of Materials Science and Engineering, Stanford University, Stanford, California 94305, USA.

*Correspondence to: zychen@stanford.edu, zxshen@stanford.edu

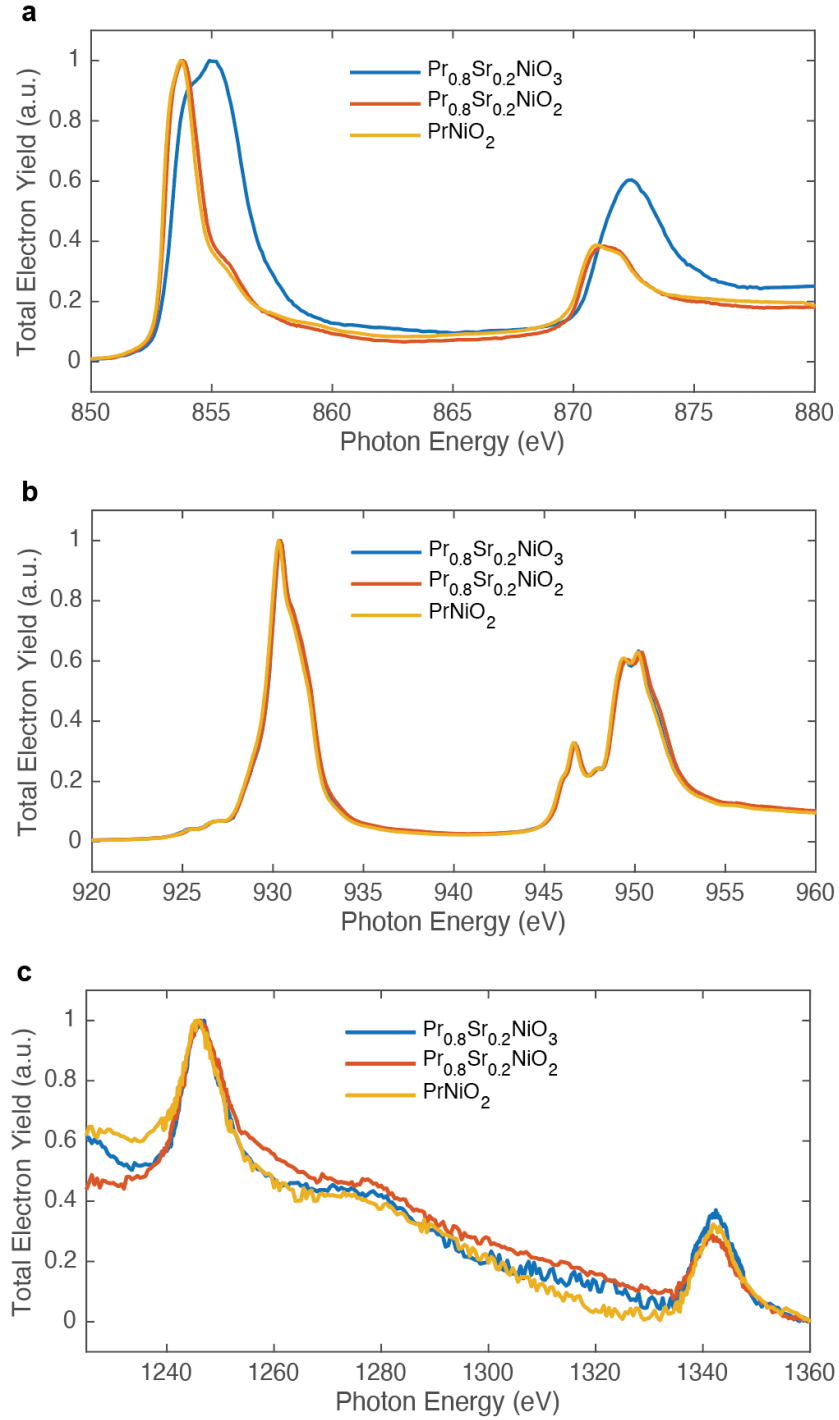


Figure S1 | XAS spectra of the three samples near Ni $L_{2,3}$, Pr $M_{4,5}$, and Pr $M_{2,3}$ edges are shown in panels **a**, **b**, and **c**, respectively. The Pr $M_{2,3}$ XAS peaks are broad and weak such that the resonant photoemission enhancement for Pr $5d$ states near E_F is below measurement detectable level.

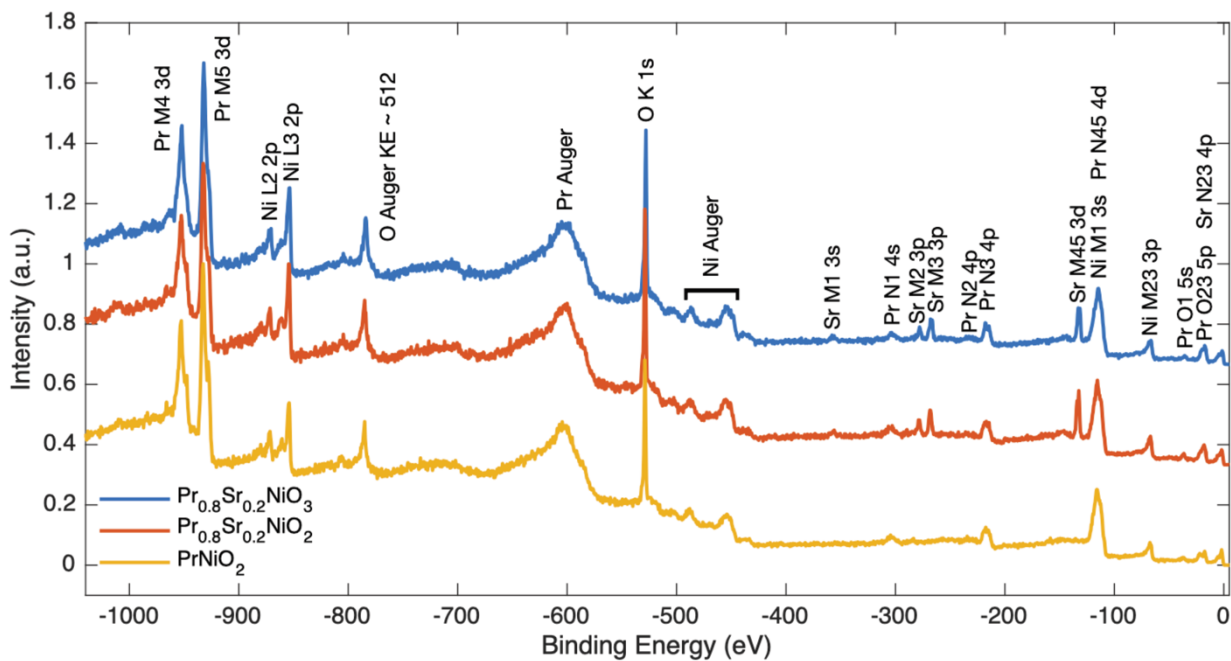


Figure S2 | Wide range XPS for the three samples measured with photon energy 1300 eV.

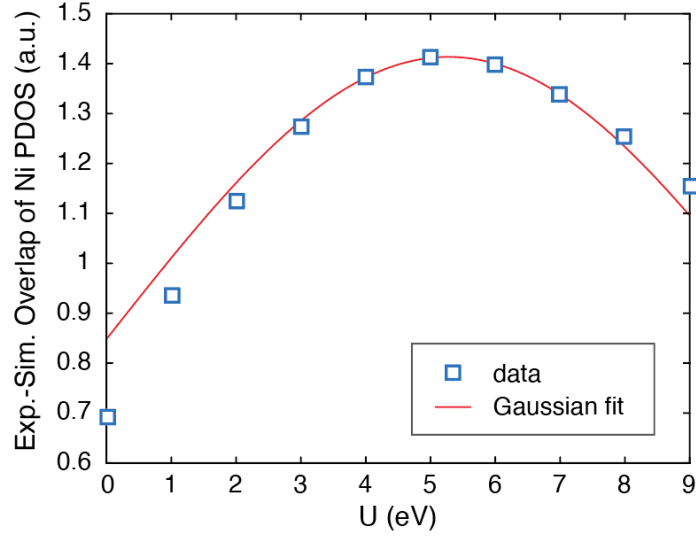


Figure S3 | Overlapped area between experimental Ni partial DOS based on Gaussian peak fitting and LDA+U simulated Ni partial DOS as a function of Hubbard U. Blue squares are data calculated from normalized partial DOS. Red curve is a Gaussian peak fit to the blue squares near the peak. The fitted mean is $U = 5.3$ eV, with 95% confidence bound being 0.3 eV. We estimate the error to be a combined effect from both the Gaussian fitting and finite data interval: $\Delta U \sim \sqrt{(0.3^2 + 1^2)} = 1.0$ eV. Thus, we estimate the peak position of this overlap $U = (5 \pm 1)$ eV.

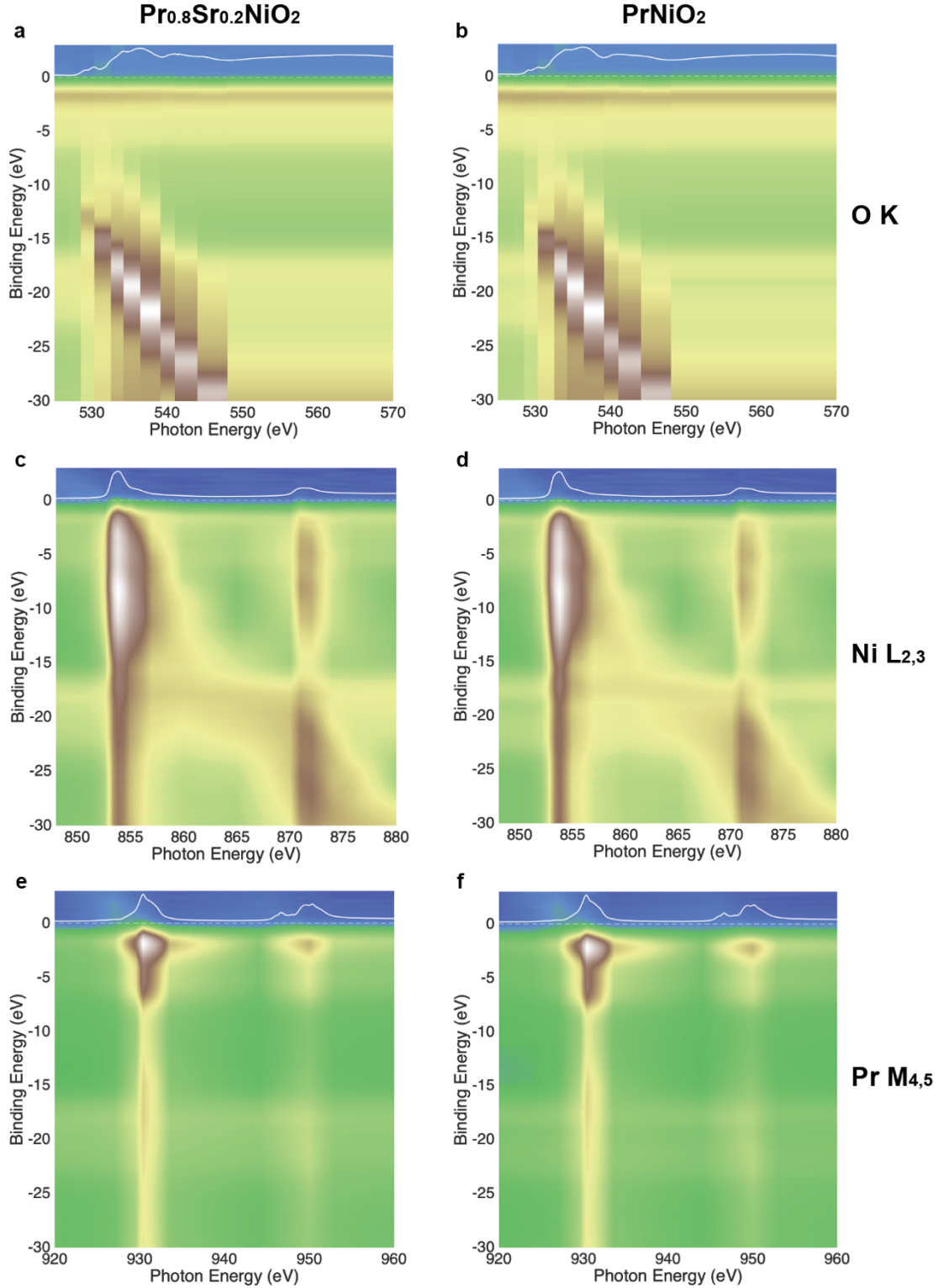


Figure S3 | Photoemission spectra of infinite layer nickelates at different photon energies in color plots, for O K (a,b), Ni L_{2,3} (c,d), and Pr M_{4,5} (e,f), respectively. Near O K edge, only Auger signal can be seen. Near Pr M_{4,5} edge, there is no Auger signal interference. The resonant enhancement near the Pr M_{4,5} edge indicates the existence of Pr 4*f* states in the valence band.